IEEE Access
Multidisciplinary | Rapid Review | Open Access Journal

Received December 7, 2018, accepted March 25, 2019, date of publication April 12, 2019, date of current version April 29, 2019.

Digital Object Identifier 10.1109/ACCESS.2019.2910830

Dynamic Analysis and Mechanical Structure Improvement of Submersible Rotor

XIAOHE RAN[1,2], (Student Member, IEEE), MENG ZHAO[1], JING SHANG[1,2], (Member, IEEE), AND CHUN HE[1]

[1]Department of Electrical Engineering, Harbin Institute of Technology, Harbin 150006, China
[2]State Key Laboratory of Robotics and Systems, Harbin Institute of Technology, Harbin 150006, China

Corresponding author: Jing Shang (Shangjing@hit.edu.cn)

This work was supported in part by the State Key Laboratory of Robotics and Systems SKLRS201812B.

ABSTRACT In order to enhance interference immunity and reduce the breakage of rotating shafts (rotors) which happens frequently especially in submersible permanent magnet synchronous motor (PMSM) applications, first a typical rotor structure is established serving as the comparative object, and then two improved schemes with optimal mechanical structure are proposed. Rotor strength, rotor stiffness, and the influence of unilateral magnetic pull on the rotor deflection are calculated analytically. The modal simulation, stress field simulation, and unilateral magnetic pull simulation are analyzed using finite element method (FEM). Position deviation and bending deformation of the rotor caused by the unilateral magnetic pulling force is taken into account to improve the simulation accuracy. The simulation results illustrate that the submersible rotor improved by the proposed schemes presents more excellent stiffness and strength performance compared with the traditional scheme, which indicates that the proposed schemes have important reference values for the structural design of submersible rotor.

INDEX TERMS Submersible motor shaft, fatigue life, dynamic model, ultra slender permanent magnet motor, electromagnetic vibration, shaft torsion deformation.

I. INTRODUCTION

Submersible motors play a decisive role in the quality and life of the submersible screw pump system. In the process of oil recovery, the breakage of the submersible motor rotor occurs frequently. It has been revealed that the main cause of rotor fatigue failure is low frequency fatigue damage, which is related to the structural parameters of permanent magnet synchronous motor (PMSM) [1]. The most effective way to reduce the fracture of rotating shaft is to improve the low frequency resonance point [1]–[3].

Several analytical methods are proposed to analyze mechanical characteristics, such as of structure deformation caused by axial electromagnetic force [4]–[7]. Based on the Maxwell stress tensor method, Kim *et al.* [8] proposed some analytical methods to calculate the radial force, and gave a guideline to reduce noise and vibration of PM-SynRM. Cao *et al.* [9] summarized the mechanical characteristics of the linear switched reluctance motors (LSRM), and the results illustrated that mover platforms were most prone to deformation even within normal force range. Ring and shell theory was used to analyze the natural frequencies of stator structures, and the feasibility in analyzing natural frequencies was verified by experimental methods [10]. The axial electromagnetic force may cause deflection and affect the machine's reliability. The finite element method was used to analyze natural frequencies of different structures of induction motors [11], [12]. The responses of dominant radial force waves were calculated separately by coupling structural and electromagnetic FEM, and these responses were superposed to assess the noise of the machines within operating range [13]. Liang *et al.* [14] provided a comprehensive investigation into the electromagnetic vibration associated with the sideband harmonic components introduced by a space vector pulse width modulation applied in integral-slot permanent magnet synchronous machine (PMSM) drives. The resonance phenomenon occurred when the rotating frequency was close to the natural frequency of the rotor, and then vibration resulted in the unevenly magnetic gap and also produced a unilateral magnetic pull force, which affected the motor output ultimately [15]. The main orders of tested noise were explained by the theoretical analysis, and it was

The associate editor coordinating the review of this manuscript and approving it for publication was Ramani Kannan.

found that the zeroth spatial order axial force is dominant for the generation of the vibration and noise in axial-flux motors. Wang *et al.* [16] provided guidance for the design of low-noise axial-flux motors. Considering rotor vibrations and thermal expansion during operation, a more accurate mechanical stress result was obtained, and the result was verified using experimental method [17]. The influence of geometric structures on modals and natural frequencies were taken into consideration, and then the effect of lamination shapes on vibrations of switched reluctance motors were studied. The effects of boundary condition on vibration and noise were taken into consideration in [18]–[20]. It had been found that the critical motor speed would increase and speed range would also expand as the stiffness of the rotor increase, and the influence of rotor stiffness coefficient on low critical speed of rotor system was studied in [21]. In order to reduce the electromagnetic vibration, Hong *et al.* [22] presented a new method by sticking a copper ring on the permanent magnet pole of a permanent magnet brush DC (PMBDC) motor, and the results showed that the vibration during motor acceleration processes reduces by up to 40% compared with motors.

At present, ensuring the safe operation of the submersible screw pump production system is one of engineering application research focuses, and it is of great significance to the development of the oil recovery industry [23]. In this paper, a novel safety design method is proposed to avoid motor failure caused by resonance or excessive local deflection. The contributions of this paper are as follows:

(1) Based on modal theory and stiffness theory, a typical rotor structure is established serving as the comparative object, and then two optimal schemes are proposed to instruct the structure design of submersible rotor.

(2) To promote the simulation accuracy, the position deviation and bending deformation caused by the unilateral magnetic pulling force are considered in FEM simulations, which is very helpful for engineering applications.

(3) Finally, the relationship between unilateral magnetic pull force and axis deflection is revealed, and its correctness is verified by simulation results.

II. ANALYSIS THEORY OF ROTOR SYSTEM

A. MODAL ANALYSIS FINITE ELEMENT THEORY

The modal analysis method has high practicability and can solve complex structural vibration problems. Modal analysis methods combined with computer-aided design (CAD) can make the analysis results more realistic, and are widely used in the engineering design and development stage.

In modal analysis, the relationship among modal $\{\phi_i\}$ and vibration frequency ω_i and model can expressed as:

$$([K] - \omega_i[M])\{\phi_i\} = 0 \tag{1}$$

where [K] is the modal stiffness matrix, M is the mass matrix. The system dynamics equation of motion can expressed as:

$$[M]\{x''\} + [C]\{x'\} + [K]\{x\} = \{F(t)\} \tag{2}$$

where $[C]$ is the damping matrix, and $\{F(t)\}$ is the force matrices. If $\{F(t)\} = 0$, then:

$$[M]\{x''\} + [C]\{x'\} + [K]\{x\} = 0 \tag{3}$$

In practical engineering applications, the material of the rotor is made of alloy steel, and the system damping is negligible. At this time, it is considered that $[C] = 0$, then:

$$[M]\{x''\} + [K]\{x\} = 0 \tag{4}$$

$\{\phi\} = \{0\}$ is one of the solutions, at which point all nodes of the structure are at rest. Solving non-zero solutions must satisfy the following formula:

$$\det([K] - \omega^2[M]) = 0 \tag{5}$$

The square root of eigenvalue ω_i is the natural frequency of free vibration of structure. The eigenvector $\{\phi_i\}$ is the modal vector corresponding to ω_i. The solution of this differential equation is more complex. Generally, the eigenvalue is solved by the FEM.

B. ROTOR STRENGTH CALCULATION

The mechanical properties of the material 40CrMnMo are shown in Table 1:

TABLE 1. Allowable stress of rotor material.

Classification	Symbol	Value (Units)
Section-Compressive stress	τ_{cs}	548.4 (Mpa)
Shear stress	τ_{mu}	211.1 (Mpa)
Compressive bending stress	τ_{cb}	365.7 (Mpa)

The maximum shear stress of the rotor cross section is:

$$\tau_m = \frac{Q}{A} \leq [\tau_m] \tag{6}$$

$$[\tau_m] = \frac{\tau_{mu}}{n_\tau} \tag{7}$$

where Q is the shear force; A is the shear plane area; τ_{mu} is the critical value of shear stress, and n_τ is the shear safety factor. When designing the rotor shear stress, sufficient margin should be left in consideration of the overload capability of the motor.

C. ROTOR STIFFNESS CALCULATION

In order to meet the stiffness requirements, the relative torsion angle on the unit length of the rotor is limited to a certain range during design.

$$\theta = T/GI_p \tag{8}$$

$$\theta \leq \theta' \tag{9}$$

where θ is the relative twist angle for unit length; T is the torque; GI_p is the torsional stiffness. θ' is the permissible relative twist angle for unit length.

When $\theta' = 0.25 \sim 0.5(^\circ)/m$, the rotor is a precision mechanical shaft; when $\theta' = 0.5 \sim 1.0(^o)/m$, it is a general drive shaft. The rated torque of the motor is 429.7Nm, and the maximum torque multiplier is 2.65. It should be designed to take into account the $T_{\max}$ (maximum torque) that can be withstood at the moment of starting.

D. CALCULATION OF THE INFLUENCE OF UNILATERAL MAGNETIC PULL ON THE ROTOR DEFLECTION

In the manufacturing process of slender structure motor, there are errors in the installation of stator and rotor, which lead to eccentricity between stator and rotor, and produce unilateral magnetic pull force, which makes the shaft deflect and bend, and increases the deflection of the motor, which seriously affects the output performance of the motor. Therefore, the influence of unilateral magnetic pull force on the mechanical structure of the motor should be considered in the design.

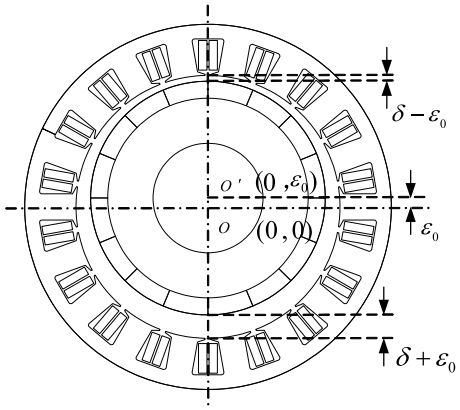

FIGURE 1. Rotor eccentric structure of submersible motor.

When the center of gravity of the rotating axis moves up ε_0 mm from the stator center, the upper air gap in the vertical direction becomes $\delta - e_0$ and the lower air gap becomes $\delta + e_0$. Therefore, the gap magnetic density $B_{\delta 1}$ of the upper air gap will increase, and the gap magnetic density $B_{\delta 2}$ of the lower decrease correspondingly. The gap magnetic density of different sizes on both sides will produce magnetic tension that can't be counteracted each other. At this time, the magnitude of the difference between the two sides of the gap magnetic tension is the magnitude of the unilateral magnetic tension. The unilateral magnetic pull produced by the motor is expressed as:

$$P_{M0} = \frac{\beta \pi D l_{ef}}{\delta} \cdot \frac{B_\delta^2}{2\mu_0} \varepsilon_0 = K_0 \varepsilon_0 \tag{10}$$

where β is the empirical coefficients (1.05-1.25); D is the outer diameter of rotor core (mm); l_{ef} is the motor shaft length (mm); B_δ is the air gap magnetic density (T); δ is the unilateral air gap length (mm); μ_0 is vacuum permeability; K_0 is the magnetic tensile stiffness (N/mm); ε_0 is the initial eccentricity (mm).

Under the influence of this unilateral magnetic pull, the deflection of the rotating shaft increases to:

$$f' = P_0/K = f_\Omega + P_0/Q \tag{11}$$

where f' is the deflection; K is the stiffness; Q is the rotor weight; f_Ω Deflection caused by rotor weight.

The formula for K is:

$$K = \frac{48EI}{L_{ef}^3} \tag{12}$$

where K is the shaft bending stiffness (N/mm); E is the material elastic modulus (MPa); I is the central moment of inertia of the shaft ($m \cdot kg \cdot s^2$); L_{ef} is the distance between bearings on the rotor (cm).

As the deflection increases, the unilateral magnetic tension increases to:

$$P_0' = P_0 + f_0/\varepsilon_0 \tag{13}$$

As the deflection increases, the motor deflection continues to increase to:

$$f'' = P_0'/K \tag{14}$$

Additional deflection is generated under the action of unilateral magnetic tension f, which continues to cause additional unilateral magnetic tension. With the increase of the elastic force of the rotating shaft, the deflection caused by the magnetic tension gradually decreases, and finally the elastic force of the rotating shaft is balanced. The total stable deflection due to the magnetic pull should be as follows:

$$f = f' + f'' + f''' \ldots = \frac{\varepsilon_0}{\varepsilon_0 - f'} \times f' = \frac{\varepsilon_0 K_0}{K - K_0} \tag{15}$$

The total deflection of the rotating shaft is equal to the sum of the deflection caused by the unilateral magnetic pull force of the rotor (f_δ), the weight of the rotor (f_Q) and the load at the extension end of the shaft (f_v).

$$f_z = f_\delta + f_Q + f_v \tag{16}$$

According to the engineering, the motor deflection is controlled within 10% of the length of the air gap.

III. ANALYSIS AND CALCULATION MODEL OF ROTOR DYNAMICS

A. ANALYSIS OF ROTOR WORKING CHARACTERISTICS

The rotor is subjected to bending moment and torque when the motor starts. While increasing the stiffness and strength of the rotor, the size and quality of the motor should be minimized. Fixed with centralized bearing and thrust bearing, the deformation range of the motor can be limited and the stress of the motor can be shared. Alloy steel with better mechanical properties is used to reduce the occurrence of rotor fracture accidents. Carbon steel and alloy steel are mainly used for rotor materials. The mechanical parameters are demonstrated in Table 2.

The submersible motor works in the vertical direction and has high bearing stiffness. The influence of bending moment

TABLE 2. Mechanical properties of materials.

Material	Alloy steel	Ss304	Symbol (Units)
Elastic Modulus	2.10×10^{11}	1.95×10^{11}	E (N/m^2)
Poisson's ratio	0.3	0.247	λ
Density	7930	7950	ρ (kg/m^3)
Yield Strength	355	205	σ_s (N/m^2)

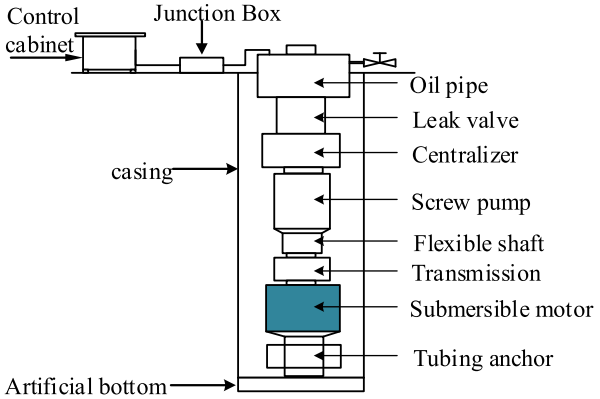

FIGURE 2. Submersible screw pump system.

FIGURE 3. Three dimensional model of rotor system.

on the rotor is far less than that of torque. The calculation on bending moment can be neglected.

In order to ensure the normal operation of the motor under low speed and heavy load, the design of the rotor dynamic characteristics during start-up should be considered to reduce the possibility of damage or breakage. When vibration occurs, the ends of the rotor is susceptible to damage caused by cyclic stress. To avoid vibration, the natural frequencies and mode shapes of the rotor should be predicted before the motor is put into use. Ensure the actual rotor speed is much smaller than the critical speed. The submersible motor generally works in a vertical manner, and the submersible screw pump system is shown in Figure 2.

The simplified finite element model is shown in Figure 3.

The thrust bearing model is shown in Figure 4.

Based on the finite element method (FEM), the geometric model, physical characteristics and complex boundary attributes of the rotor are simplified, which can effectively reduce the calculation time.

B. MODAL SIMULATION RESULT POST-PROCESSING

Based on the mechanical simulation platform for modal analysis, according to the previous engineering experience,

FIGURE 4. Model of thrust bearing.

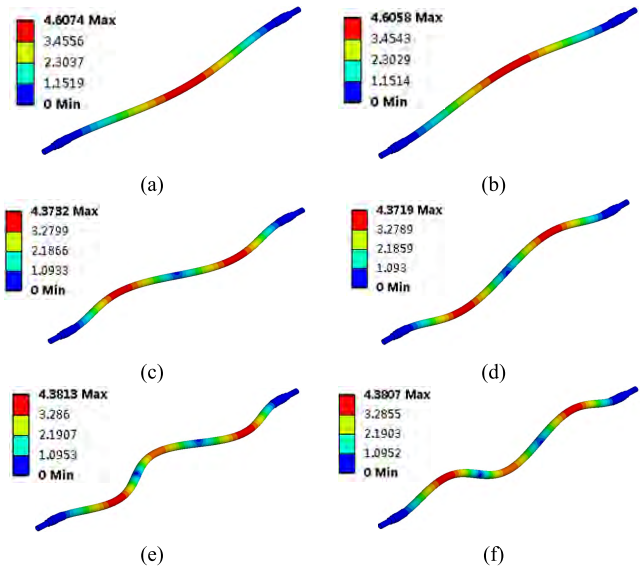

FIGURE 5. Rotary low-order mode shape of rotor. (a) First order mode. (b) Second order mode. (c) Third order mode. (d) Fourth order mode. (e) Fifth order mode. (f) Sixth order mode.

TABLE 3. FEM analysis results.

Modal order	Natural frequency(Hz)	Mode shape	Direction	Maximum deformation(mm)
1	37.899	Bending	YZ plane	4.607
2	38.309	Bending	XZ plane	4.605
3	103.65	vibration	Z axis	4.373
4	104.76	Torsional	XZ plane	4.371
5	201.18	Torsional	YZ plane	4.381
6	203.30	vibration	Z axis	4.380

the low-order modes are mainly analyzed in detail, extracted the first six modes, as shown in Figure 5:

Collate Figure 5 data as demonstrated in Table 3.

Analysis the frequency (Table 3) and the mode (Figure 5) yield in the following conclusions:

(1) The rated operating frequency of the motor is 133.33 Hz, and the first order natural frequency of the rotor is 37.899 Hz. When the motor is started, the rotation frequency rises from 0 to 133.33 Hz, and resonance occurs when it is close to the natural frequency. The motor generates noise and the dynamic characteristics are significantly degraded.

(2) Analyze the second-order vibration mode of the rotor, and the vibration occurs at the suction port end. The third-order and fourth-order vibration modes indicate that the

vibration position is transferred to the eccentric section of the rotor. Under actual working conditions, the middle part of the rotor is prone to deformation. The stiffness and strength of the middle portion of the rotor should be strengthened.

(3) According to the rotor stability theory, when the rotation speed of the rotor is $n \leq 0.7(n_1$ is the first-order critical speed), the rotor can be regarded as a rigid axis, and the motor runs smoothly; when $n > 0.7n_1$, the rotor is regarded as a flexible shaft, and the motor is easy to resonate. The motor generates noise, and the friction between the rotor and the stator occurs.

The simulation results illustrated that the rotor is a flexible shaft, the rated running speed of the motor exceeds the safe range, the resonance causes the rotor to collide with the stator, the failure rate increases, and the motor cannot output safely and stably.

C. STRESS FIELD SIMULATION RESULTS POST-PROCESSING

Using FEM to solve the solution, the electromagnetic torque and core weight are applied as loads. The equivalent stress and equivalent deformation of the rotor are as follows:

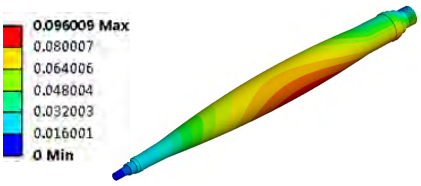

FIGURE 6. Equivalent deformation of rotor.

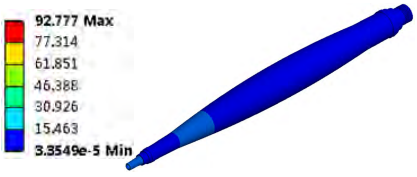

FIGURE 7. Equivalent stress of rotor.

It is found that the gravity has small influence on the rotor deformation. The maximum deformation position is in the rear part of the rotor (the maximum allowable deflection is 10% of the air gap, about 0.1 mm), close to the dangerous range, the structure needs to be improved.

D. ANALYSIS OF UNILATERAL MAGNETIC PULL ON THE MOTOR

The calculated results demonstrated that the unilateral magnetic pull force is 494.5N and the rotor deflection is 0.075mm. In order to verify the theoretical calculation value, establish the simulation model, the supporting constraints are applied at the position of the centralized bearing and the equivalent force load is applied at the rotor sheath. The equivalent stress and equivalent deformation are as follows:

The maximum equivalent deformation is 0.0776mm and the maximum equivalent stress is 8.803Mpa. The unilateral

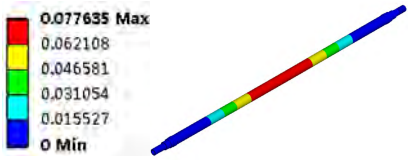

FIGURE 8. Equivalent deformation of rotor.

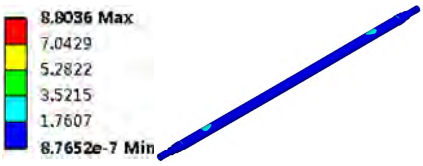

FIGURE 9. Equivalent stress of rotor.

FIGURE 10. Model 1: add a centralizer bearing in the middle part of the most easily deformed shaft.

FIGURE 11. Model 2: add two centralizer bearings at the full length of the 1/3 from the two ends of the shaft.

magnetic pulling force causes the rotor to be radially deformed, and the central portion of the rotor is deformed to the maximum, which is consistent with the theoretical verification and the actual situation. The analysis found that the initial unilateral magnetic pulling force has a great influence on the rotor. It is necessary to pay attention to improve the process precision and minimize the assembly error. Otherwise, the long-term use will increase the noise vibration of the motor and accelerate the wear of the motor.

IV. CHARACTERISTIC ANALYSIS OF OPTIMIZATION MODEL

A. ESTABLISHMENT OF OPTIMIZATION MODEL

Basing on modal analysis finite element theory, two optimization models are established. The number of centralized bearings in the models is different, and the bearing position distribution is shown in the figure.

At the same time, the influence of centralized bearing on the deformation and natural frequency of rotor is analyzed.

B. MODAL SIMULATION RESULT POST-PROCESSING

The first six natural frequencies and modes of Model 1 are shown in Figure 12:

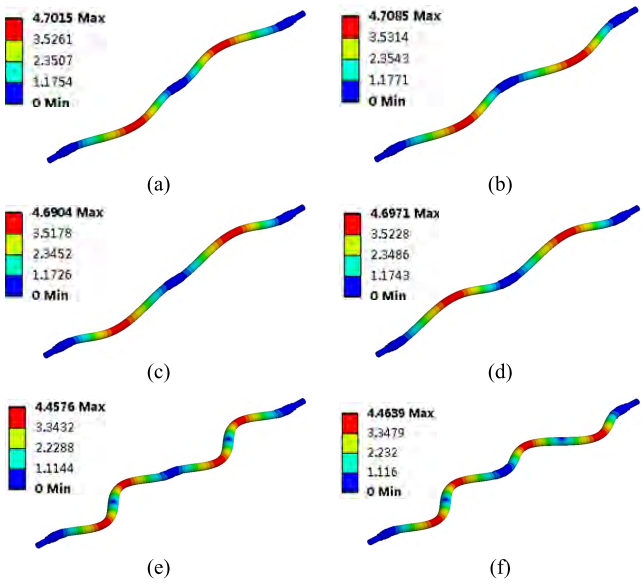

FIGURE 12. Rotary low-order mode shape of Model 1. (a) First order mode. (b) Second order mode. (c) Third order mode. (d) Fourth order mode. (e) Fifth order mode. (f) Sixth order mode.

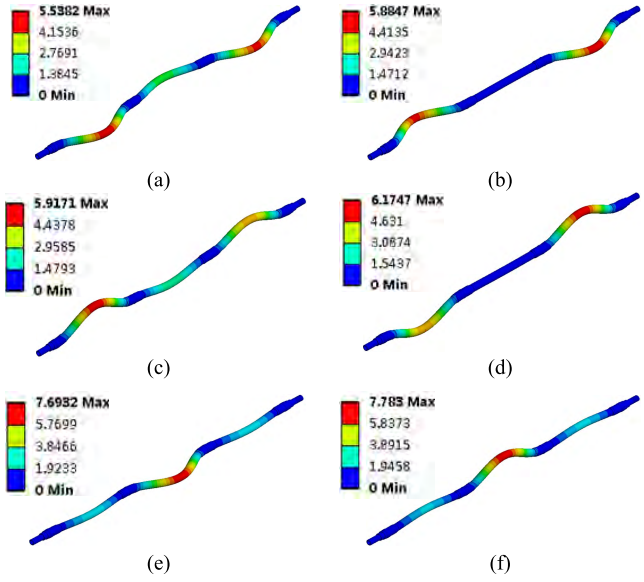

FIGURE 13. Rotary low-order mode shape of Model 2. (a) First order mode. (b) Second order mode. (c) Third order mode. (d) Fourth order mode. (e) Fifth order mode. (f) Sixth order mode.

The first six natural frequencies and modes of Model 2 are shown in Figure 13:

The results of natural frequencies are shown in Table 4 and Table 5.

When model 2 is used, the natural frequencies of the six modes are close, and continuing to join the righting bearing will not significantly increase the natural frequency of the motor. The second low-order natural frequency of the model is higher than the rated frequency of the motor, which avoids motor resonance and friction.

In this paper $n_N = 1000$r/min, the two motor shafts of the model are rigid shafts, and the resonance process does not occur during the starting process, and the motor can run smoothly.

TABLE 4. FEM analysis results of Model 1.

Modal order	Natural frequency (Hz)	Critical speed (r/min)	Maximum deformation (mm)
1	159.37	1195.28	4.7015
2	160.31	1202.33	4.7085
3	160.90	1206.75	4.6904
4	161.87	1214.03	4.6971
5	425.18	3188.85	4.4576
6	427.77	3208.28	4.4639

TABLE 5. FEM analysis results of Model 2.

Modal order	Natural frequency (Hz)	Critical speed (r/min)	Maximum deformation (mm)
1	361.25	2709.38	5.5382
2	362.97	2722.28	5.8847
3	364.29	2732.18	5.9171
4	365.65	2742.38	6.1741
5	368.65	2764.88	7.6932
6	371.69	2787.68	7.7830

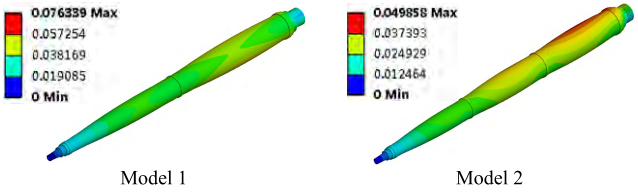

FIGURE 14. Equivalent deformation of rotor.

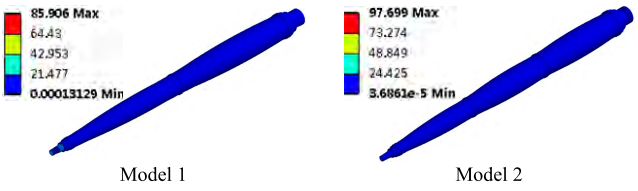

FIGURE 15. Equivalent stress of rotor.

C. STRESS FIELD SIMULATION RESULTS POST-PROCESSING

Using FEM to solve the solution, the equivalent stress and equivalent deformation distribution of the rotor are as follows:

Analysis of Figure 14 and Figure 15, the maximum strain position of the rotor is in the back part, and the strength of the end of the suction port is greater than the stress, so that the system can operate safely. The maximum deformation and equivalent stress are shown in Table 6.

The maximum equivalent force of the rotor at rated torque is 83.946MPa, which is in line with the bearing material receiving range. After several tests, the range of torque applied under deflection is calculated.

TABLE 6. Parameters of maximum deformation and equivalent stress.

Model	Maximum deformation	Maximum equivalent stress
1	159.37mm	1195.28Mpa
2	427.77mm	3208.28Mpa

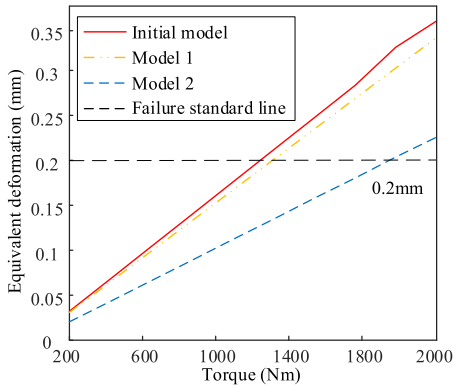

FIGURE 16. Curve of maximum equivalent deformation of torque.

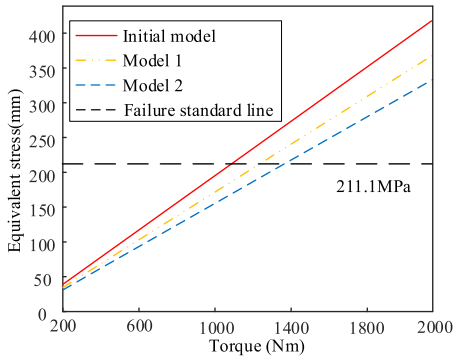

FIGURE 17. Curve of maximum equivalent stress of torque.

In Figure 16 and Figure 17, the strain and stress of the rotor increase linearly with the change of the torque. Because the submersible motor is placed vertically, the stress generated by gravity in the radial direction of the shaft is approximately zero. The equivalent deformation and pressure caused by gravity during motor starting are negligible. Analyze the shaft's strain range, find the maximum strain position of the motor, use the righting bearing to constrain the shaft deformation, share the shaft stress, and effectively avoid the friction between the stator and the rotor.

D. ANALYSIS OF UNILATERAL MAGNETIC PULL ON THE MOTOR

The calculated unilateral magnetic pull force is 494.5N, and the shaft deflection is 0.065mm, which is less than 0.1 times the air gap length, the motor can work safely. In order to verify the theoretical calculation, the rotor simulation model is established, the support constraint is applied at the rotor support bearing position according to the constraint condition, and the effective load such as the unilateral magnetic pull force is applied at the motor shaft sheath position. The results are as follows:

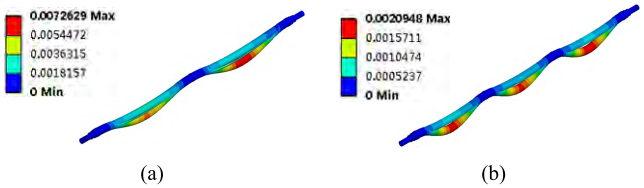

FIGURE 18. Equivalent deformation. (a) Model 1. (b) Model 2.

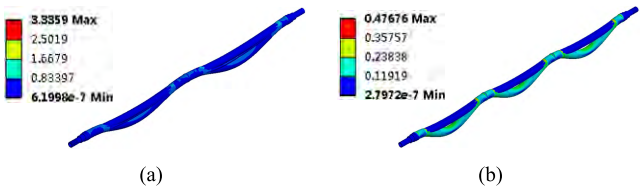

FIGURE 19. Equivalent stress. (a) Model 1. (b) Model 2.

TABLE 7. Parameters of maximum stress and maximum strain.

Model	Maximum deformation	Maximum stress
1	0.0073mm	3.335mm
2	0.0021mm	0.046mm

Figure 18 illustrated that the radial deformation of the shaft is caused by unilateral magnetic pull, and the maximum deformation is in the middle position. The deformation and stress data of unilateral magnetic pull are shown in Table 7.

The deflection of the motor shaft is 0.00776mm, less than 0.1 times the air gap length, and the maximum equivalent stress is within the range of the bearing, which meets the design requirements.

It demonstrated that the initial unilateral magnetic pull has a great influence on the rotor. Long-term use will accelerate the wear and tear of the submersible motor, increase the noise and vibration. When manufacturing a motor, we should pay attention to improve the process accuracy and minimize the assembly error.

V. CONCLUSION

Basing on modal analysis finite element theory and stiffness theory, the paper proposes two schemes that are used to instruct the structure design of submersible rotor, which can reduce the uneven air gap caused by the deflection of the rotor shaft. The position deviation and bending deformation of the rotor caused by the unilateral magnetic pulling force are considered in the proposed schemes. Simulation results indicate that the submersible rotor designed by the proposed schemes offers a good performance in stiffness and strength, and the vibration frequency can be predicted to avoid resonance, which has a promising application value in submersible rotor's structural design in practical engineering.

REFERENCES

[1] D. Kim, M. D. Noh, and Y. W. Park, "Unbalanced magnetic forces due to rotor eccentricity in a toroidally wound BLDC motor," *IEEE Trans. Magn.*, vol. 52, no. 7, pp. 1–4, Jul. 2016.

[2] H.-J. Shin, J.-Y. Choi, H.-I. Park, and S.-M. Jang, "Vibration analysis and measurements through prediction of electromagnetic vibration sources of permanent magnet synchronous motor based on analytical magnetic field calculations," *IEEE Trans. Magn.*, vol. 48, no. 11, pp. 4216–4219, Nov. 2012.

[3] Y. Lu *et al.*, "Electromagnetic force and vibration analysis of permanent-magnet-assisted synchronous reluctance machines," *IEEE Trans. Ind. Appl.*, vol. 54, no. 5, pp. 4246–4256, Oct. 2018.

[4] B. Xu, C. Xiang, Y. Qin, P. Ding, and M. Dong, "Semi-active vibration control for in-wheel switched reluctance motor driven electric vehicle with dynamic vibration absorbing structures: Concept and validation," *IEEE Access*, vol. 6, pp. 60274–60285, 2018.

[5] K. Yamazaki and Y. Kato, "Iron loss analysis of interior permanent magnet synchronous motors by considering mechanical stress and deformation of stators and rotors," *IEEE Trans. Magn.*, vol. 50, no. 2, pp. 909–912, Feb. 2014.

[6] M. Qiao, C. Jiang, y. Zhu, and G. Li, "Research on design method and electromagnetic vibration of six-phase fractional-slot concentrated-winding PM motor suitable for ship propulsion," *IEEE Access*, vol. 4, pp. 8535–8543, 2016. doi: 10.1109/access.2016.2636341.

[7] C. Liu, G. Cao, S. Huang, and Y. Liu, "Modal analysis and linear static structure analysis of linear switched reluctance motor," in *Proc. 4th IEEE Int. Conf. Inf. Sci. Technol.*, Shenzhen, China, Apr. 2014, pp. 467–470.

[8] D. Y. Kim, J. K. Nam, and G. H. Jang, "Reduction of magnetically induced vibration of a spoke-type IPM motor using magnetomechanical coupled analysis and optimization," *IEEE Trans. Magn.*, vol. 49, no. 9, pp. 5097–5105, Sep. 2013.

[9] Y. Cao, L. Yu, and H. Jia, "Rotor mechanical stress and deformation analysis of coreless stator axial-flux permanentmagnet machines," in *Proc. IEEE Int. Magn. Conf. (INTERMAG)*, May 2015, p. 1.

[10] G. Verez and C. Espanet, "Natural frequencies analytical modeling of small industrial radial flux permanent magnet motors," in *Proc. 18th Int. Conf. Elect. Mach. Syst. (ICEMS)*, Oct. 2015, pp. 1963–1969.

[11] F. Ishibashi, K. Kamimoto, T. Hayashi, S. Noda, and K. Itomi, "Natural frequency of stator core of small induction motor," *IEE Proc.-Electr. Power Appl.*, vol. 150, no. 2, pp. 210–214, Mar. 2003.

[12] F. Ishibashi, M. Matsushita, S. Noda, and K. Tonoki, "Change of mechanical natural frequencies of induction motor," *IEEE Trans. Ind. Appl.*, vol. 46, no. 3, pp. 922–927, Jun. 2010.

[13] X. Li, S. Huang, Q. Zhang, and Y. Dai, "Electromagnetic noise assessment for EV's PM driving machines," in *Proc. 17th Int. Conf. Elect. Mach. Syst. (ICEMS)*, Oct. 2014, pp. 1552–1555.

[14] W. Liang, P. C. Luk, and W. Fei, "Analytical investigation of sideband electromagnetic vibration in integral-slot PMSM drive with SVPWM technique," *IEEE Trans. Power Electron.*, vol. 32, no. 6, pp. 4785–4795, Jun. 2017.

[15] Y. Zhang and Y. U. Haichun, "Reliability of electrical submersible pumping unit," *Acta Petrolei Sinica*, vol. 24, no. 4, pp. 103–107, 2003.

[16] K. Wang, X. Wang, and M. Tian, "The modal analysis of the stator of the interior permanent magnet machine," in *Proc. 20th Int. Conf. Elect. Mach. Syst. (ICEMS)*, Sydney, NSW, Australia, Aug. 2017, pp. 1–5.

[17] F. Chai, Y. Li, P. Liang, and Y. Pei, "Calculation of the maximum mechanical stress on the rotor of interior permanent-magnet synchronous motors," *IEEE Trans. Ind. Electron.*, vol. 63, no. 6, pp. 3420–3432, Jun. 2016.

[18] X. Zhou and Y. Zhang, "A new linear ultrasonic motor using hybrid longitudinal vibration mode," *IEEE Access*, vol. 4, pp. 10158–10165, 2016.

[19] W. Deng and S. Zuo, "Axial force and vibroacoustic analysis of external-rotor axial-flux motors," *IEEE Trans. Ind. Electron.*, vol. 65, no. 3, pp. 2018–2030, Mar. 2018.

[20] W. Cai and P. Pillay, "Design and control of switched reluctance motors with low vibration and noise," in *Proc. IEEE Int. Electr. Mach. Drives Conf.*, Antalya, Turkey, May 2007, pp. 1324–1331.

[21] S. Singhal, K. V. Singh, and A. Hyder, "Effect of laminated core on rotor mode shape of large high speed induction motor," in *Proc. IEEE Int. Electr. Mach. Drives Conf. (IEMDC)*, Niagara Falls, ON, Canada, May 2011, pp. 1557–1562.

[22] J. Hong, S. Wang, Y. Sun, and H. Cao, "An effective method with copper ring for vibration reduction in permanent magnet brush DC motors," *IEEE Trans. Magn.*, vol. 54, no. 11, pp. 1–5, Nov. 2018.

[23] X. Liang, O. Ghoreishi, and W. Xu, "Downhole tool design for conditional monitoring of electrical submersible motors in oil field facilities," *IEEE Trans. Ind. Appl.*, vol. 53, no. 3, pp. 3164–3174, Jun. 2017.

XIAOHE RAN was born in Harbin, Heilongjiang, China, in 1994. She received the B.S. and M.S. degrees in electrical engineering from the Harbin Institute of Technology, China, where she is currently pursuing the Ph.D. degree with the Laboratory of Microelectric Motor. Her current research interests include motor design and drive control.

MENG ZHAO was born in 1974. He received the Ph.D. degree from the Department of Electrical Engineering, Harbin Institute of Technology, where he is currently an Associate Professor. His research interests include magnetic fluid seal, design of the motor magnetic field, and so on.

JING SHANG was born in 1968. He received the Ph.D. degree with the Department of Electrical Engineering, Harbin Institute of Technology, where he is currently a Professor. His research interests include small and special motor and controlling, and so on.

CHUN HE was born in Zunyi, Guizhou, China, in 1995. He received the B.S. degree in electrical engineering from the Harbin Institute of Technology, China, where he is currently pursuing the master's degree with the Laboratory of Microelectric Motor. His current research interests include model predictive control in power converters and electrical drives.